

Two-Dimensional Conductive Ni-HAB as a Catalyst for the Electrochemical Oxygen Reduction Reaction

Jihye Park,[#] Zhihua Chen,[#] Raul A. Flores,[#] Gustaf Wallnerström, Ambarish Kulkarni, Jens K. Nørskov,^{*} Thomas F. Jaramillo,^{*} and Zhenan Bao^{*}



Cite This: *ACS Appl. Mater. Interfaces* 2020, 12, 39074–39081



Read Online

ACCESS |



Metrics & More



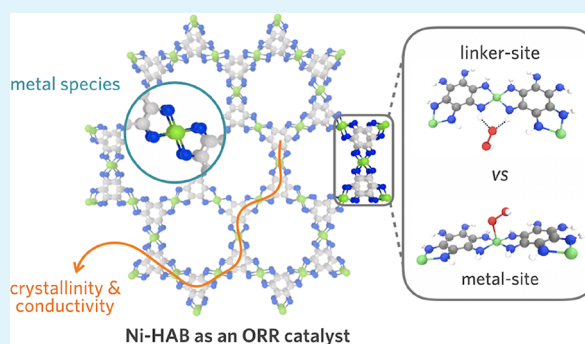
Article Recommendations



Supporting Information

ABSTRACT: Catalytic systems whose properties can be systematically tuned via changes in synthesis conditions are highly desirable for the next-generation catalyst design and optimization. Herein, we present a two-dimensional (2D) conductive metal–organic framework consisting of $M-N_4$ units ($M = Ni, Cu$) and a hexaaminobenzene (HAB) linker as a catalyst for the oxygen reduction reaction. By varying synthetic conditions, we prepared two Ni-HAB catalysts with different crystallinities, resulting in catalytic systems with different electric conductivities, electrochemical activity, and stability. We show that crystallinity has a positive impact on conductivity and demonstrate that this improved crystallinity/conductivity improves the catalytic performance of our model system. Additionally, density functional theory simulations were performed to probe the origin of M-HAB's catalytic activity, and they suggest that M-HAB's organic linker acts as the active site with the role of the metal being to modulate the linker sites' binding strength.

KEYWORDS: metal–organic frameworks, electrical conductivity, electrocatalysis, active sites, oxygen reduction reactions, density functional theory



INTRODUCTION

The oxygen reduction reaction (ORR) is an important electrochemical process for fuel cell applications ($4e^-$ process) and the electrochemical production of hydrogen peroxide ($2e^-$ process) as an energy efficient alternative to the traditional anthraquinone-based process. Noble metal-based catalysts such as Pt and Pd-Hg are the current state-of-the-art for the $4e^-$ and $2e^-$ process, respectively, exhibiting low overpotentials and high stabilities. Despite their outstanding performance, their scalability is limited by the scarcity and expense of the noble metals.¹ This is particularly true for the electrochemical production of hydrogen peroxide, which due to the poor stability of the product, has to be performed under relatively milder conditions and with a different experimental setup than the $4e^-$ ORR.^{2,3} Thus, intensive research efforts have been devoted to developing cost-effective catalysts based on earth-abundant elements, such as nonprecious metal/metal oxide catalysts, carbides, nitrides, and metal-free carbon materials. Central to these efforts is the engineering of catalysts with optimal ORR binding energetics and highly accessible, dense active sites for high catalytic performance.

Previously, low-cost molecular systems containing $M-N_4$ macrocyclic complexes have been demonstrated as high performing ORR catalysts^{4,5} where the $M-N_4$ motif represents a catalytically active site composed of a single metal species

coordinated to four nitrogens. Although molecular catalysts with $M-N_4$ units have exhibited notable activity,⁶ the low electrical conductivity of molecular catalysts requires a large amount of conductive additives (e.g., carbon black), resulting in a significant dilution of active site density on a per mass basis. Considering this, a catalyst design that can maximize the density of $M-N_4$ units in a conducting matrix would be highly desirable.⁷ To address this issue, pyrolysis of $M-N_4$ containing precursors into a carbon matrix has been attempted to enhance the stability and electrical conductivity of the catalyst.⁸ However, after pyrolysis, the chemical nature and conformation of the active centers are often extensively altered with unidentifiable defects, which presents a challenge in determining the nature of the active sites.⁹ Thus, a bottom-up synthesis approach with well-defined building blocks would be ideal to realize $M-N_4$ rich catalysts due to a much more benign synthesis procedure compared to pyrolysis.

Received: May 23, 2020

Accepted: August 4, 2020

Published: August 4, 2020



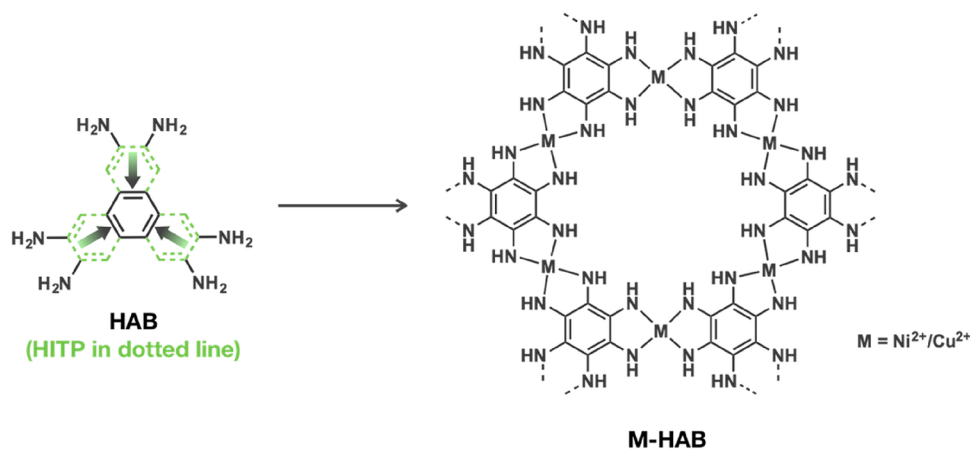


Figure 1. Synthetic scheme for the c-MOF M-HAB. Left: chemical structure of the molecular linker utilized herein, hexaaminobenzene (HAB, black), with the structure of a larger topological analog hexaaminotriphenylene (HITP, green) shown for comparison. Right: c-MOF M-HAB structure; the use of a relatively small HAB linker results in a framework with a high density of active sites.

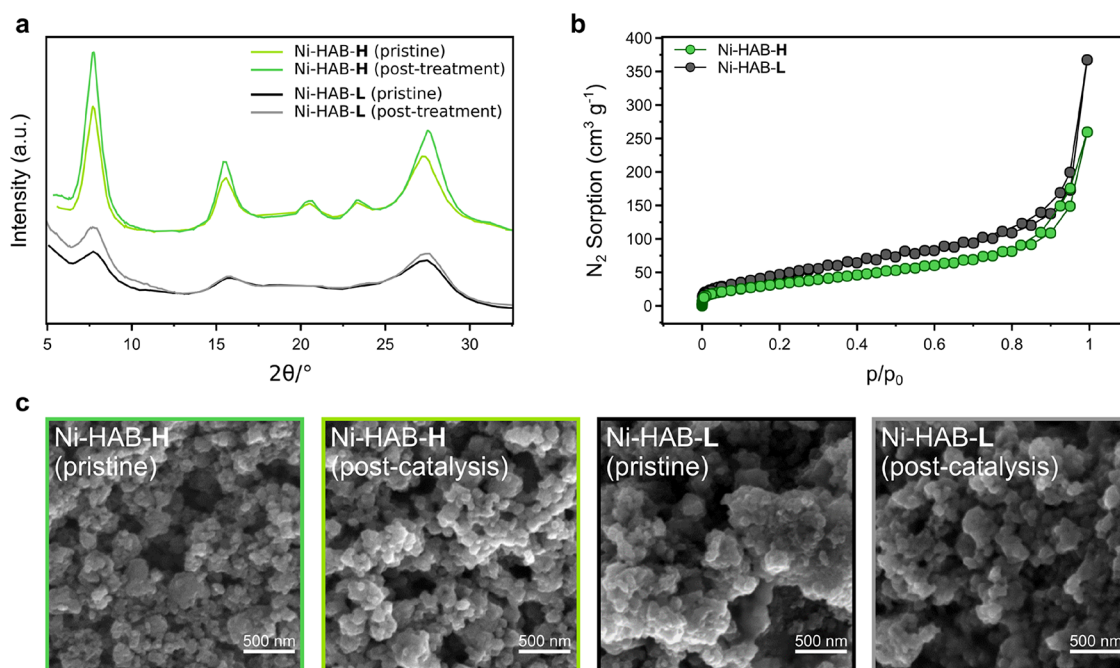


Figure 2. (a) Comparison of PXRD patterns of Ni-HAB samples before and after the buffer treatment (0.1 M KOH buffer). (b) N₂ sorption isotherms of Ni-HAB-H/Ni-HAB-L. BET surface area L: 180 m²/g, H: 129 m²/g. (c) SEM images of M-HAB before and after electrochemical testing.

Herein, we report a new synthesis procedure to obtain highly conductive two-dimensional (2D) metal–organic frameworks (c-MOFs) with dense M-N₄ units, namely, M-HAB (M = Cu, Ni; HAB = hexaaminobenzene), as catalysts for the ORR.¹⁰ M-HAB is a highly tunable materials system, and by varying synthesis conditions, we demonstrate that M-HAB can provide a great platform for the study of ORR activity with respect to the identity of the metal species and the catalyst's electrical conductivity.^{11–14}

A similar 2D MOF based on the hexaaminotriphenylene (HITP) linker and Ni(II) node, which has a larger triphenylene-based unit (Figure 1), has been previously reported.^{15,16} With a combination of experimental results and theoretical calculations, we found that the identity of the metal plays a key role in determining the catalytic activity of M-HAB by modulating the electronic environment around the highly

conjugated organic networks. Previously, theoretical calculations on Cu- and Ni-HAB were performed but neglected any active site other than the direct metal cation.¹⁷ Our theoretical analysis, however, suggests that the preferred active site is in-plane with the 2D c-MOF matrix with ORR intermediates binding strongly to multiple N-H groups of the M-N₄ moieties (Figure 4). Such sites (referred to as linker sites herein) exploit the large degree of conjugation in the MOF framework, which facilitates the formation of strong hydrogen-bond interactions with the ORR intermediates. We also studied the effect of conductivity in the same framework by tuning the synthetic conditions. We successfully prepared Ni-HAB catalysts with improved crystallinity and electrical conductivity. High crystallinity was found to correlate positively with ORR activity with high onset potentials of 0.8 V vs RHE to achieve 1 mA/cm² in a rotating disk electrode (RDE) setup. The catalyst

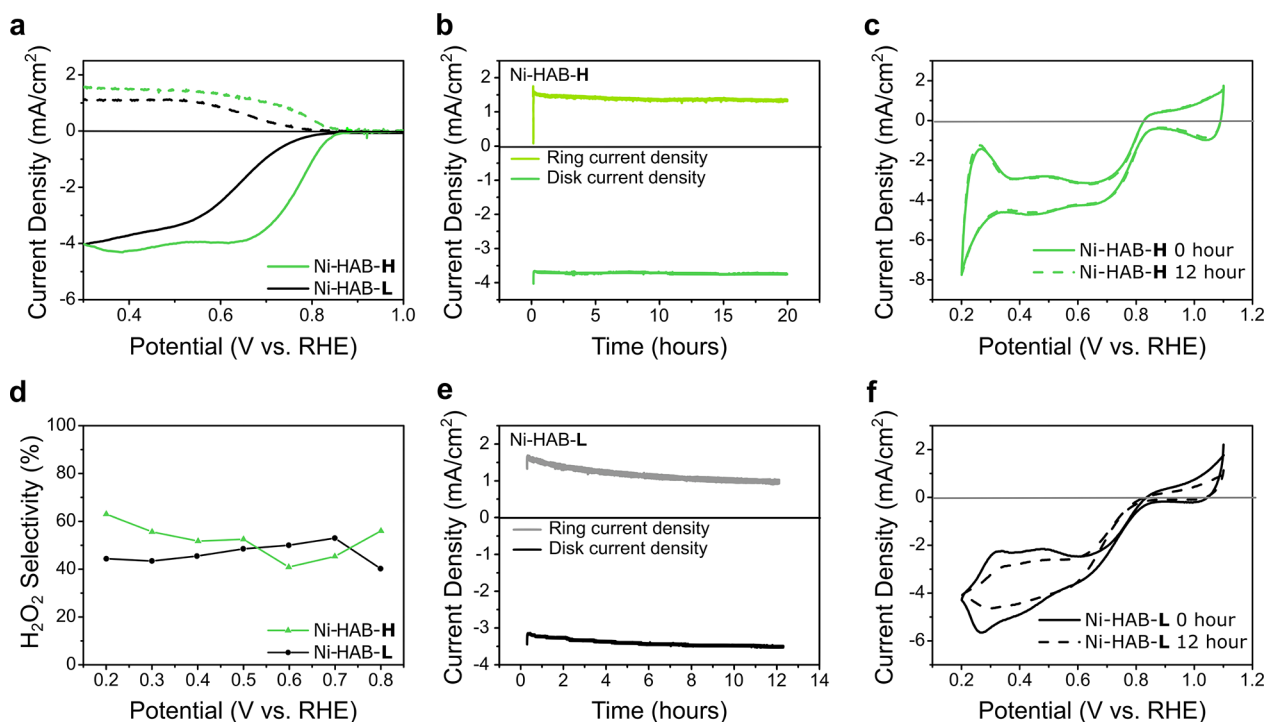


Figure 3. (a) RRDE measurements for Ni-HAB-H and Ni-HAB-L (the oxidative H_2O_2 ring currents are indicated by dashed lines). (b) Steady-state potentiostatic measurements at a saturation current of 0.5 V vs RHE for Ni-HAB-H. (c) RDE measurements for Ni-HAB-H before and after 12 h of steady-state potentiostatic measurements at a saturation current at 0.5 V vs RHE. (d) Selectivity from the RRDE measurements for Ni-HAB systems. (e) Steady-state potentiostatic measurements at a saturation current of 0.5 V vs RHE for Ni-HAB-L. (f) RDE measurements for Ni-HAB-L before and after 12 h of steady-state potentiostatic measurements at a saturation current of 0.5 V vs RHE. The measurements in panels (a, b, d, e) show the H_2O_2 current at $\times 3.9$ for detection efficiency.

demonstrates stability for over 20 h at 0.5 V vs RHE applied potential with a moderate selectivity toward hydrogen peroxide.

RESULTS AND DISCUSSION

Synthesis of Ni-HAB-H and Ni-HAB-L. We recently reported 2D conductive MOFs, namely, M-HAB (M = Ni, Cu), where the HAB linkers are bridged by transition metal species with square planar geometry (Figure 1).¹⁰ Due to the smaller size of the HAB linker compared to its topological analog, HITP, the M-HAB system can achieve a denser packing of M- N_4 units with an underlying (2,3)-honeycomb topology.¹⁸

The structure of synthesized Ni- and Cu-HAB products were confirmed by powder X-ray diffractions (PXRD), which show a good agreement with our previously reported 2D honeycomb eclipsed structures (Figure 2a).¹⁰ The previously reported synthetic conditions used 100% H_2O as the solvent, which yielded Ni-HAB with much poorer crystallinity compared to Cu-HAB. Thus, we further optimized the synthesis conditions to yield a Ni-HAB product with crystallinity comparable to Cu-HAB, which allows for a fairer control of the effects of crystallinity on the ORR activity. The Ni-HAB product with higher crystallinity was synthesized by using dimethyl formaldehyde (DMF) (1:1, v/v) at an elevated temperature (75 °C) and will henceforth be referred to as Ni-HAB-H, while the lower crystalline product will be referred as Ni-HAB-L. Having M-HAB catalysts synthesized with comparable crystallinity, we tested their chemical and electrochemical stability and found that, under harsh electrolyte treatment (0.1 M KOH), the crystallinity of Cu-HAB severely

degrades over 24 h (Figure S2). Similarly, Cu-HAB suffers from an electrochemical degradation, especially at lower potential (Figure S3). For instance, Cu-HAB generated a large irreversible current at around 0.3 V vs RHE, which is indicative of degradation, considering that the mass transport-limited current for the full $4e^-$ ORR process is only about 6 mA/cm^2 .¹⁹

Having characterized their identical structures evidenced by PXRD patterns and similar particle sizes, we tested the chemical stability of Ni-HAB-H and Ni-HAB-L in the same electrolyte solution used for electrochemical testing (0.1 M KOH in water). Typically, the chemical stability of MOFs is highly governed by the strength of the M-L bonds, and thus, the metal species plays an important role in determining its chemical stability. Ni-HAB shows much better stability than Cu-HAB under the electrochemical testing condition indicated by the well-maintained PXRD patterns after the buffer treatment.

ORR Activity of Ni-HAB-H and Ni-HAB-L. Cyclic voltammograms (CV) of the catalysts were measured on a glassy carbon rotating ring disk electrode (RRDE) setup mentioned in the Supporting Information with a spin rate of 1600 rpm. Catalysts were prepared by an ink-based drop-casting process. The net current presented was calculated by subtracting the double-layer capacitance under high N_2 flow with the absence of O_2 . While scanning electron microscopy images reveal that there was no noticeable changes in size and morphology after the catalytic testing (Figure 2c), for the Ni-HAB-H sample, the onset potential was determined to be 0.8 V vs RHE with fast kinetics, reaching a mass transport-limited current at 0.7 V vs RHE. Despite the similarity in the

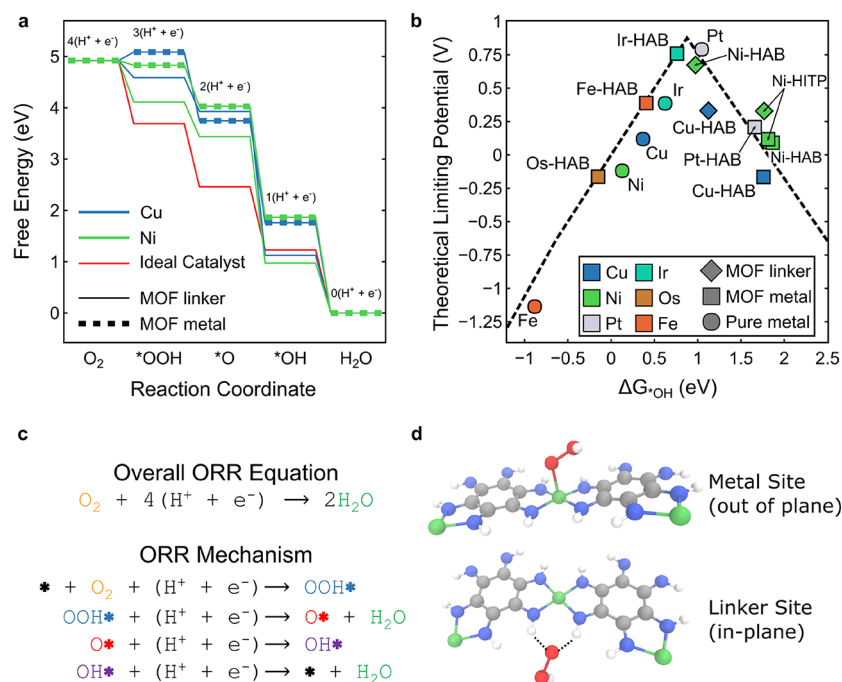


Figure 4. (a) Free energy diagram of Cu- and Ni-HAB for the four-electron-transfer ORR mechanism with the ideal catalyst pathway shown in red. The linker-mediated pathway is shown in solid lines, while the metal active sites are dotted. (b) Theoretical ORR limiting potential volcano plot with the systems computed as well as other systems of interest obtained from literature. The volcano plot was determined by assuming “universal” scaling relations ($\Delta G_{\text{OOH}} = \Delta G_{\text{OH}} + 3.2$ and $\Delta G_{\text{*O}} = 2\Delta G_{\text{OH}}$).²³ ORR data on Fe, Ni, Cu, Ir, and Pt were obtained from literature,²³ while the data for Os-HAB, Fe-HAB, Ir-HAB, and Pt-HAB were reproduced from Yang *et al.*²⁴ (c) Overall ORR chemical equation and the four-electron-transfer associative ORR mechanism. Under the associative ORR mechanism, the reaction proceeds through three primary oxygen-based intermediates: *OOH, *O, and *OH. (d) Chemical structure of Ni-HAB (oxygen: red; hydrogen: white; nitrogen: blue; nickel: green). Metal and in-plane linker-mediated binding modes are shown. The energetics of all computed structures as well as the corresponding structure files can be found at [Catalysis-Hub.org](https://catalysis-hub.org).^{25,26}

selectivity, however, the onset potential of Ni-HAB-L is delayed compared to Ni-HAB-H. For instance, an onset potential of 0.7 V vs RHE and even higher overpotentials were required to reach the limiting current, indicative of the relatively lower activity and slower kinetics for Ni-HAB-L. This is likely attributed to less exposure of active sites on the surface of Ni-HAB-L and/or slow mass transport. Because the high-crystallinity product (Ni-HAB-H) contains more crystalline domains with better accessibility than the low crystalline product, the more amorphous features of Ni-HAB-L results in a lower density of exposed/accessible active sites as well as a slower mass transport. Additionally, the ring current indicates that both Ni-HAB-H and Ni-HAB-L show a moderate selectivity toward H_2O_2 of around 50% (Figure 3a,d), despite the electrochemical active surface areas (ECSA) of the Ni-HAB-H and Ni-HAB-L being comparable (Figure S1). Therefore, the enhancement in the reactivity of Ni-HAB-H relative to Ni-HAB-L is most likely due to the enhancement in crystallinity and conductivity rather than differences in intrinsic active site activity.

Stability of Ni-HAB during the ORR. Electrochemical stability under operating conditions is a crucial requirement for catalyst performance. Steady-state potentiostatic measurements at a saturation current of 0.5 V vs RHE show that nearly 100% of the initial current density was retained over the 20 h of potential hold for both the ring and disk currents on Ni-HAB-H (Figure 3b). This indicates a more promising result compared with the previously reported Ni-HITP structures with respect to their onset potential and the rate to reach the mass transport-limited current.¹⁰ Additionally, a thorough

stability test was performed at a lower operating potential, which is at a much harsher reducing potential than what is reported for Ni-HITP. Both the ring and disk currents are recorded and have shown no major changes in both the activity and selectivity over the 20 h testing period. Cyclic voltammetry measurements before and after the 12 h potential hold show no change in the entire potential region for the ORR (Figure 3c,f). The lower crystallinity sample, Ni-HAB-L, however, showed a notable decrease in the ORR and H_2O_2 current over a potential hold of 12 h and irreversible redox features, as shown by cyclic voltammetry in the 0.2–1.1 V vs RHE voltage window. One plausible decomposition mechanism for MOFs is the over-reduction of the metal center, which causes further leaching of the metal species out of the framework. Additionally, we believe that, due to the lower effective density of intrinsic $M-N_4$ active sites and the relatively lower conductivity of Ni-HAB-L compared to its counterpart Ni-HAB-H, the electron transport (the assumed rate determining step) is inhibited, resulting in slower onset kinetics.

Electrical Conductivity of M-HAB. The electrical conductivities of bulk Ni-HAB catalysts were measured using four-point probe measurements with pelletized powders. As expected, the more crystalline Ni-HAB-H exhibited a conductivity over an order of magnitude larger than that of Ni-HAB-L (conductivity of 1.050 and 0.086 S/cm for Ni-HAB-H and Ni-HAB-L, respectively). It is worth noting that Ni-HAB-H presents a slightly lower Brunauer–Emmett–Teller (BET) surface area of ~ 130 m^2/g than that of Ni-HAB-L (~ 200 m^2/g), which may be ascribed to a lower contribution from the mesoporous regime arising from inter-particle

packing (Figure 2b). Therefore, the improvement in the ORR performance is less likely due to surface area contributions but from the enhanced conductivity that results in better electron transport to the active centers. As a result, despite the similarity in the nature of the active center (Figures 3a and 4b), Ni-HAB-H demonstrated a faster increase in the current toward the mass transport-limited region. The enhanced stability also leads to improved cyclability and clearer redox features, which are believed to be related to the reversible redox process upon the active centers.

Theoretical Activity of M-HAB. Density functional theory (DFT) calculations were performed on M-HAB and M-HITP systems to probe the origin of Ni-HAB's electrochemical activity. Adsorption free energies of the intermediate species for the four-electron associative ORR mechanism (see Figure 4c for mechanism) were computed from DFT energies and vibrational free energy corrections according to previously developed models^{20,21} (see the Supporting Information for further computational details). By employing the computational hydrogen electrode, the free energy diagrams of all systems were constructed (Figure 4a) from which the thermodynamic limiting potential (LP) (highest potential at which the ORR remains exergonic) was evaluated.²² The LP has an indirect, but positive, correlation with the experimentally observed onset potentials and as such is a useful metric by which to benchmark simulated catalyst materials. The theoretical LPs are summarized in an ORR activity volcano plot (see Figure 4b), which relates the LP to the adsorption free energy of the *OH intermediate (ΔG_{*OH}).

Two sites were considered as active centers in the M-HAB/HITP frameworks, the more conventional metal active site and an organic linker-mediated active site (see Figure 4d). The linker-mediated active site was motivated by recent works on the ORR activity of M-HITP MOFs, a closely related system to M-HAB with larger nanopores and a honeycomb structure.^{15,27} Other notable theoretical works on the ORR activity of 2D frameworks include the work by Xiao *et al.* into $TM_3(HHTP)_2$ and Zhang *et al.*'s work on the hydroxylated analog to M-HAB.^{28,29} Additional DFT calculations were performed on Ni-HITP as well as Cu-HAB to elucidate the effects of the linker and metal identity on the ORR activity.

Figure 4a shows that both Ni- and Cu-HAB are generally weak binding (higher adsorption energies) materials relative to the ideal ORR catalyst (red line). In particular, the metal binding site is considerably weak binding with the ΔG_{*OOH} , ΔG_{*O} , and ΔG_{*OH} under binding by 1.27, 1.43, and 0.58 eV, relative to the ideal ORR catalyst. Interestingly, the in-plane linker binding site (Figure 4d, bottom) demonstrates significantly stronger binding compared to the out-of-plane metal site (Figure 4d, top) with *OOH and *OH binding of 0.69 eV more strongly at the linker sites. The unusually strong linker binding energies could be due to the phenomenon of "strong resonance-assisted hydrogen bonding" observed for other highly conjugated organic systems and/or the fact that the relatively small honeycomb pore of M-HAB allows for up to four hydrogen bonds with the adsorbates (see the Supporting Information, Section S4.4 for further analysis of the linker binding site for Ni-HAB).³⁰ Due to the linker site's stronger oxygen binding, the theoretical limiting potential is enhanced from 0.1 to 0.67 V for Ni-HAB (experimental onset of 0.8 V vs RHE at 1 mA/cm²) and from -0.2 to 0.3 V for Cu-HAB. The stronger and more favorable ORR energetics at the organic linker thus support a linker-mediated mechanism.

The ORR activity volcano (Figure 4b) relates the ORR LP to the adsorption energy of ΔG_{*OH} by invoking scaling relations to express the adsorption energies of *OOH and *O in terms of ΔG_{*OH} .^{31,32} Figure 4b shows that the metal binding sites for Ni-HAB, Cu-HAB, and Ni-HITP (squares) lie to the right of the volcano maximum ($\Delta G_{*OH} = 0.86$ eV) and therefore bind *OH too weakly to have high activity. Conversely, the linker-mediated mechanism on Ni-HAB has strengthened *OH binding, resulting in a high LP (0.67 V) that is comparable to platinum. Comparing the M-HAB and M-HITP motifs for M = Ni, Figure 4b shows that the activity on the metal site is similar between these two MOF structures with limiting potentials of 0.10 and 0.12 V vs RHE and *OH free energies of adsorption ($\Delta G_{ads,*OH}$) of 1.87 and 1.81 eV, respectively. Conversely, the activity and *OH adsorption free energies vary drastically between the linker centered pathway [$\Delta \Delta G_{ads,*OH}(HITP - HAB) = 0.8$ eV and $\Delta LP(HITP - HAB) = 0.3$ V vs RHE], indicating that the linker may play an important role in modulating the ORR activity in 2D c-MOFs containing M-N₄ sites. Additional computational data for M-HAB was included from a recent report²⁴ for M = Os, Fe, Ir, and Pt, and the activities for the corresponding pure metal crystals are reproduced from literature.²² In general, the pure metal crystals bind much stronger than the corresponding M-HAB catalyst, which presents an interesting avenue to activate transition metals on the strong binding side of the volcano by supporting them into an HAB framework.

CONCLUSIONS

Herein, we demonstrated the synthesis of M-HAB (M = Ni, Cu) catalysts of varying crystallinity/conductivity via synthetic modulation and successfully studied the contribution of crystallinity/conductivity toward the ORR behavior of these systems. Ni-HAB-H exhibits an earlier onset potential compared to the catalyst with poorer crystallinity, possibly due to the fewer defects and better electron conduction in Ni-HAB-H. The catalytic performance was largely dependent on the metal species with Cu-HAB being much less active and stable under the given electrochemical potential. Additionally, our theoretical modeling suggests that the in-plane linker site acts as the active center. In addition to being a promising candidate for ORR fuel cell applications, the favorable stability of Ni-HAB may also allow for the elucidation of the ORR pathway on the M-HAB platform via future *in situ* studies.

EXPERIMENTAL SECTION

Materials and Instrumentations. All reagents and starting materials were purchased from Sigma-Aldrich or Alfa Aesar and were used without further purification. Hexaaminobenzene (HAB) was synthesized according to literature.³³ Powder X-ray diffraction was carried out on a BRUKER D8 venture single crystal diffractometer equipped with a Cu-sealed tube ($\lambda = 1.54$ Å) using capillary at 50 kV and 1 mA. Scanning electron microscopy (SEM) analysis was performed on a field emission-scanning electron microscope (Magellan 400 XHR) at 5 kV. Gas adsorption was measured using a Micromeritics ASAP 2020, and the BET surface areas were calculated using its software. Electrical conductivity measurements were carried out using a Keithley 4200 SCS parameter analyzer.

Synthesis of Ni-HAB-H with High Crystallinity. A solution of 105 mg (0.36 mmol) of nickel nitrate hexahydrate [$Ni(NO_3)_2 \cdot 6H_2O$] was dissolved in a mixture of 25 mL of DMF (dimethylformamide) and 20 mL of water in a round bottom flask. The solution was preheated on an oil bath at 75 °C for 15 min. Afterward, 50 mg of HAB-3 HCl (0.18 mmol) in 5 mL of H₂O was added into the nickel

nitrate solution while stirring in open air. Aqueous ammonium hydroxide (NH₄OH; 180 μL, 6 M) (1.08 mmol, 6 equiv to HAB) was added immediately. This mixture was stirred in air for 2 h at 75 °C. The resulting black powder was filtered and subsequently washed with water. Finally, the solid was washed with acetone and dried under vacuum at 80 °C for 2 h.

Synthesis of Ni-HAB-L with Low Crystallinity. A solution of 21 mg (0.072 mmol) of nickel nitrate hexahydrate [Ni(NO₃)₂·6H₂O] was dissolved in 5 mL of water. HAB-3 HCl (10 mg, 0.036 mmol) in 10 mL of H₂O was then added into the nickel nitrate solution under stirring in open air. Aqueous ammonium hydroxide (NH₄OH; 60 μL, 6 M) (0.36 mmol, 10 equiv to HAB) was added immediately. This mixture was stirred in an open vial for an hour at room temperature. The resulting black powder was filtered and then washed with water. Finally, the solid was washed with acetone and dried under vacuum at 80 °C for 2 h.

Electrochemical and Chemical Stability Tests. Stability tests of M-HAB were performed in a KOH aqueous buffer solution (0.1 M). As-synthesized samples (~10 mg) were suspended in 2 mL of 0.1 M KOH for 24 h at room temperature. Afterward, the sample was further washed with water and acetone. All samples were subsequently treated by typical activation procedures mentioned previously. After being dried under vacuum for 3 h at 75 °C, the samples were degassed on an ASAP2420 adsorption system for 2 h at 80 °C. These samples were then measured for N₂ sorption at 77 K. Finally, all samples were characterized by powder X-ray diffraction to confirm the crystallinity (Figure 2a).

Electrochemical stability of the materials was tested by holding the potential at 0.5 V vs RHE for 12 h, and the current was measured during the process. Three regular 10 mV/s scans between 0.2 and 1.1 V vs RHE were conducted before and after the 12 h potential hold to ascertain the change in activity over time.

Electrochemical Characterizations. All electrochemical testings were carried out under alkaline conditions with 0.1 M KOH in water (1 kg P250-1 Potassium Hydroxide Certified ACS, Fisher Chemical). The pH was measured to be 13 by a pH meter unless otherwise noted. The measurements were conducted through either a rotation ring disk electrode (RRDE) or rotation disk electrode (RDE) setup in a four/three-electrode setup utilizing a graphite rod counter electrode with an Ag/AgCl reference electrode.

Catalysts were prepared through an ink-based drop-casting process. For testing in alkaline solutions, the working electrode ink was prepared by mixing 1 mg of the catalyst, 98 μL of ethanol, and 2 μL of cation-exchanged Nafion 117 solution (Sigma-Aldrich). The resulting catalyst ink (10 μL) was then drop-casted onto a glassy carbon (GC) disk working electrode (Sigradur G HTW Hochtemperatur-Werkstoffe GmbH) by two rounds of casting, 5 μL each time. The glassy carbon disks were rotated at an initial rate of 300 rpm and advanced to 600 rpm to obtain a final catalyst loading of 0.51 mg/cm².

Electrochemical measurements were carried out by sweeping the disk potential between 0.2 V and 1.1 V vs RHE at 10 mV/s while holding the Pt ring electrode at 1.2 V vs RHE to oxidize H₂O₂ species formed on the disc electrode, allowing for ORR product quantification. The potential scale was calibrated to the reversible hydrogen electrode (RHE) using a Pt wire (Sigma-Aldrich) as the working electrode in an H₂-saturated electrolyte, and a value of 0.959 V, referenced to RHE, was obtained. The ORR activity was determined by subtracting the current obtained in an N₂-saturated electrolyte from that obtained in an O₂-saturated electrolyte. The system's ring collection efficiency was determined to be 0.2545 using the reversible [Fe(CN)₆]^{4-/3-} redox couple (+0.36 vs SHE). The selectivity of H₂O₂ can be calculated according to eq 1

$$\text{H}_2\text{O}_2(\%) = 200 \frac{I_R/N}{I_D + I_R/N} \quad (1)$$

where I_R is the ring current, I_D is the disk current, and N is the collection efficiency.

Electrical Conductivity Measurements. The pellets (3.175 mm diameter, 200–300 μm thickness) for conductivity measurement were prepared by cold isostatic pressing using commercial pressing equipment (MTI Corporation). Electrical conductivity of pellets of Co-HAB were measured by the four-point probe method at 25 °C. A pellet was placed on a glass slide and mounted into a four-arm probe station (Lakeshore). Four tungsten tip probes made contact with the pellet at a spacing of 0.75 mm apart. The chamber was evacuated to ca. few 10⁻⁴ mbar for 24 h prior to measurement to avoid the influence of oxygen and moisture. Electrical data were collected in the dark with a Keithley 4200 SCS parameter analyzer.

Computational Methodology. Density functional theory calculations were performed for *OOH, *O, and *OH species adsorbed on M-HAB and Ni-HITP catalyst materials to compute the free energy reaction pathway for the ORR. Adsorption energies were corrected by computing entropy, zero-point energy, and heat capacity contributions of the adsorbed species under the harmonic oscillator approximation.

Theoretical limiting potentials defined by the highest positive bias at which the ORR remains thermodynamically favorable were calculated for all systems of interest and summarized in a volcano plot. Further details on the DFT methodology, calculation of adsorption free energies, and other computational methodologies can be found in the Supporting Information.

■ ASSOCIATED CONTENT

Supporting Information

The Supporting Information is available free of charge at <https://pubs.acs.org/doi/10.1021/acsami.0c09323>.

Additional supplementary figures and experimental and computational methodologies (PDF)

■ AUTHOR INFORMATION

Corresponding Authors

Jens K. Nørskov – SUNCAT Center for Interface Science and Catalysis, Department of Chemical Engineering, Stanford University, Stanford, California 94305, United States; Department of Physics, Technical University of Denmark, DK-2800 Lyngby, Denmark; Email: jkn@dtu.dk

Thomas F. Jaramillo – Department of Chemical Engineering and SUNCAT Center for Interface Science and Catalysis, Department of Chemical Engineering, Stanford University, Stanford, California 94305, United States; orcid.org/0000-0001-9900-0622; Email: jaramillo@stanford.edu

Zhenan Bao – Department of Chemical Engineering, Stanford University, Stanford, California 94305, United States; orcid.org/0000-0002-0972-1715; Email: zbao@stanford.edu

Authors

Jihye Park – Department of Chemical Engineering, Stanford University, Stanford, California 94305, United States; orcid.org/0000-0002-8644-2103

Zhihua Chen – Department of Chemical Engineering and SUNCAT Center for Interface Science and Catalysis, Department of Chemical Engineering, Stanford University, Stanford, California 94305, United States

Raul A. Flores – Department of Chemical Engineering and SUNCAT Center for Interface Science and Catalysis, Department of Chemical Engineering, Stanford University, Stanford, California 94305, United States; orcid.org/0000-0001-5047-2530

Gustaf Wallnerström – Department of Chemical Engineering, Stanford University, Stanford, California 94305, United States;

Department of Chemical Engineering, KTH Royal Institute of Technology, Stockholm 100 44, Sweden

Ambarish Kulkarni – Department of Chemical Engineering, University of California Davis, Davis, California 95616, United States

Complete contact information is available at:
<https://pubs.acs.org/10.1021/acsami.0c09323>

Author Contributions

#J.P., Z.C., and R.A.F. contributed equally to this work.

Notes

The authors declare no competing financial interest.

ACKNOWLEDGMENTS

J.P. acknowledges support from the Dreyfus Foundation Postdoctoral Fellowship for Environmental Chemistry. This work partially was supported by the Toyota Research Institute. Some of the computing for this project was performed on the Sherlock cluster. Z.B. acknowledges U.S. Department of Energy, Office of Science, Office of Basic Energy Science, via Grant DE-SC0008685 to the SUNCAT Center of Interface Science and Catalysis. We would like to thank Stanford University and the Stanford Research Computing Center for providing computational resources and support that contributed to these research results. Special thanks to Profs. Dawei Feng and Drew Higgins and Dr. Shucheng Chen for their valuable help.

REFERENCES

- (1) Bashyam, R.; Zelenay, P. A Class of Non-Precious Metal Composite Catalysts for Fuel Cells. *Nature* **2006**, *443*, 63–66.
- (2) Chen, Z.; Chen, S.; Siahrostami, S.; Chakthranont, P.; Hahn, C.; Nordlund, D.; Dimosthenis, S.; Nørskov, J. K.; Bao, Z.; Jaramillo, T. F. Development of a Reactor with Carbon Catalysts for Modular-Scale, Low-Cost Electrochemical Generation of H₂O₂. *React. Chem. Eng.* **2017**, *2*, 239–245.
- (3) Kim, H. W.; Park, H.; Roh, J. S.; Shin, J. E.; Lee, T. H.; Zhang, L.; Cho, Y. H.; Yoon, H. W.; Bukas, V. J.; Guo, J.; Park, H. B.; Han, T. H.; McCloskey, B. D. Carbon Defect Characterization of Nitrogen-Doped Reduced Graphene Oxide Electrocatalysts for the Two-Electron Oxygen Reduction Reaction. *Chem. Mater.* **2019**, *31*, 3967–3973.
- (4) Chen, Z.; Higgins, D.; Yu, A.; Zhang, L.; Zhang, J. A Review on Non-Precious Metal Electrocatalysts for PEM Fuel Cells. *Energy Environ. Sci.* **2011**, *4*, 3167–3192.
- (5) Li, Y.; Li, Q.; Wang, H.; Zhang, L.; Wilkinson, D. P.; Zhang, J. Recent Progresses in Oxygen Reduction Reaction Electrocatalysts for Electrochemical Energy Applications. *Electrochem. Energy Rev.* **2019**, *2*, 518–538.
- (6) Zagal, J. H.; Koper, M. T. M. Reactivity Descriptors for the Activity of Molecular Mn₄ Catalysts for the Oxygen Reduction Reaction. *Angew. Chem., Int. Ed.* **2016**, *55*, 14510–14521.
- (7) Kruusenberg, I.; Mondal, J.; Matisen, L.; Sammelselg, V.; Tammeveski, K. Oxygen Reduction on Graphene-Supported MN₄ Macrocycles in Alkaline Media. *Electrochem. Commun.* **2013**, *33*, 18–22.
- (8) To, J. W. F.; Ng, J. W. D.; Siahrostami, S.; Koh, A. L.; Lee, Y.; Chen, Z.; Fong, K. D.; Chen, S.; He, J.; Bae, W.-G.; Wilcox, J.; Jeong, H. Y.; Kim, K.; Studt, F.; Nørskov, J. K.; Jaramillo, T. F.; Bao, Z. High-Performance Oxygen Reduction and Evolution Carbon Catalysis: From Mechanistic Studies to Device Integration. *Nano Res.* **2017**, *10*, 1163–1177.
- (9) Chen, Y.; Ji, S.; Chen, C.; Peng, Q.; Wang, D.; Li, Y. Single-Atom Catalysts: Synthetic Strategies and Electrochemical Applications. *Joule* **2018**, *2*, 1242–1264.
- (10) Feng, D.; Lei, T.; Lukatskaya, M. R.; Park, J.; Huang, Z.; Lee, M.; Shaw, L.; Chen, S.; Yakovenko, A. A.; Kulkarni, A.; Xiao, J.; Fredrickson, K.; Tok, J. B.; Zou, X.; Cui, Y.; Bao, Z. Robust and Conductive Two-Dimensional Metal–Organic Frameworks with Exceptionally High Volumetric and Areal Capacitance. *Nat. Energy* **2018**, *3*, 30–36.
- (11) Downes, C. A.; Marinescu, S. C. Electrocatalytic Metal–Organic Frameworks for Energy Applications. *ChemSusChem* **2017**, *10*, 4374–4392.
- (12) Lahiri, N.; Lotfizadeh, N.; Tsuchikawa, R.; Deshpande, V. V.; Louie, J. Hexaaminobenzene as a Building Block for a Family of 2D Coordination Polymers. *J. Am. Chem. Soc.* **2017**, *139*, 19–22.
- (13) Jiao, L.; Wang, Y.; Jiang, H.-L.; Xu, Q. Metal–Organic Frameworks as Platforms for Catalytic Applications. *Adv. Mater.* **2018**, *30*, 1703663.
- (14) Gascon, J.; Corma, A.; Kapteijn, F.; Llabrés i Xamena, F. X. Metal Organic Framework Catalysis: Quo Vadis? *ACS Catal.* **2014**, *4*, 361–378.
- (15) Miner, E. M.; Gul, S.; Ricke, N. D.; Pastor, E.; Yano, J.; Yachandra, V. K.; Van Voorhis, T.; Dincă, M. Mechanistic Evidence for Ligand-Centered Electrocatalytic Oxygen Reduction with the Conductive MOF Ni₃(Hexaiminotriphenylene)₂. *ACS Catal.* **2017**, *7*, 7726–7731.
- (16) Miner, E. M.; Fukushima, T.; Sheberla, D.; Sun, L.; Surendranath, Y.; Dincă, M. Electrochemical Oxygen Reduction Catalysed by Ni₃(Hexaiminotriphenylene)₂. *Nat. Commun.* **2016**, *7*, 10942–10942.
- (17) Gao, G.; Waclawik, E. R.; Du, A. Computational Screening of Two-Dimensional Coordination Polymers as Efficient Catalysts for Oxygen Evolution and Reduction Reaction. *J. Catal.* **2017**, *352*, 579–585.
- (18) Sheberla, D.; Sun, L.; Blood-Forsythe, M. A.; Er, S.; Wade, C. R.; Brozek, C. K.; Aspuru-Guzik, A.; Dincă, M. High Electrical Conductivity in Ni₃(2,3,6,7,10,11-Hexaiminotriphenylene)₂, a Semi-conducting Metal–Organic Graphene Analogue. *J. Am. Chem. Soc.* **2014**, *136*, 8859–8862.
- (19) Ben Liew, K.; Daud, W. R. W.; Ghasemi, M.; Leong, J. X.; Su Lim, S.; Ismail, M. Non-Pt Catalyst as Oxygen Reduction Reaction in Microbial Fuel Cells: A Review. *Int. J. Hydrogen Energy* **2014**, *39*, 4870–4883.
- (20) Man, I. C.; Su, H.-Y.; Calle-Vallejo, F.; Hansen, H. A.; Martínez, J. I.; Inoglu, N. G.; Kitchin, J.; Jaramillo, T. F.; Nørskov, J. K.; Rossmeisl, J. Universality in Oxygen Evolution Electrocatalysis on Oxide Surfaces. *ChemCatChem* **2011**, *3*, 1159–1165.
- (21) Rossmeisl, J.; Qu, Z. W.; Zhu, H.; Kroes, G. J.; Nørskov, J. K. Electrolysis of Water on Oxide Surfaces. *J. Electroanal. Chem.* **2007**, *607*, 83–89.
- (22) Nørskov, J. K.; Rossmeisl, J.; Logadottir, A.; Lindqvist, L.; Kitchin, J. R.; Bligaard, T.; Jónsson, H. Origin of the Overpotential for Oxygen Reduction at a Fuel-Cell Cathode. *J. Phys. Chem. B* **2004**, *108*, 17886–17892.
- (23) Kulkarni, A.; Siahrostami, S.; Patel, A.; Nørskov, J. K. Understanding Catalytic Activity Trends in the Oxygen Reduction Reaction. *Chem. Rev.* **2018**, *118*, 2302–2312.
- (24) Yang, X.; Hu, Q.; Hou, X.; Mi, J.; Zhang, P. Oxygen Reduction Reaction on M₃(Hexaiminobenzene)₂: A Density Function Theory Study. *Catal. Commun.* **2018**, *115*, 17–20.
- (25) Flores, R. A. *M-HAB Surface Adsorption Dataset*; <https://www.Catalysis-Hub.Org/Publications/Park2d2019> (accessed June 1, 2020).
- (26) Winther, K. H.; Max, J.; Mamun, O.; Boes, J. R.; Nørskov, J. K.; Bajdich, M. *Catalysis-Hub.Org: An Open Electronic Structure Database for Surface Reactions*, 2018, chemrxiv.7336094.v2. *ChemRxiv* (accessed June 1, 2020).
- (27) Lian, Y.; Yang, W.; Zhang, C.; Sun, H.; Deng, Z.; Xu, W.; Song, L.; Ouyang, Z.; Wang, Z.; Guo, J.; Peng, Y. Unpaired 3d Electrons on Atomically Dispersed Cobalt Centres in Coordination Polymers Regulate Both Oxygen Reduction Reaction (Orr) Activity and Selectivity for Use in Zinc–Air Batteries. *Angew. Chem., Int. Ed.* **2020**, *59*, 286–294.

(28) Xiao, B. B.; Liu, H. Y.; Jiang, X. B.; Yu, Z. D.; Jiang, Q. A Bifunctional Two Dimensional $Tm_3(Hhpt)_2$ Monolayer and Its Variations for Oxygen Electrode Reactions. *RSC Adv.* **2017**, *7*, 54332–54340.

(29) Zhang, J.; Zhou, Z.; Wang, F.; Li, Y.; Jing, Y. Two-Dimensional Metal Hexahydroxybenzene Frameworks as Promising Electrocatalysts for an Oxygen Reduction Reaction. *ACS Sustainable Chem. Eng.* **2020**, *8*, 7472–7479.

(30) Wu, C.-H.; Ito, K.; Buytendyk, A. M.; Bowen, K. H.; Wu, J. I. Enormous Hydrogen Bond Strength Enhancement through π -Conjugation Gain: Implications for Enzyme Catalysis. *Biochemistry* **2017**, *56*, 4318–4322.

(31) Calle-Vallejo, F.; Martínez, J. I.; García-Lastra, J. M.; Rossmeisl, J.; Koper, M. T. M. Physical and Chemical Nature of the Scaling Relations between Adsorption Energies of Atoms on Metal Surfaces. *Phys. Rev. Lett.* **2012**, *108*, 116103.

(32) Abild-Pedersen, F.; Greeley, J.; Studt, F.; Rossmeisl, J.; Munter, T. R.; Moses, P. G.; Skúlason, E.; Bligaard, T.; Nørskov, J. K. Scaling Properties of Adsorption Energies for Hydrogen-Containing Molecules on Transition-Metal Surfaces. *Phys. Rev. Lett.* **2007**, *99*, 016105.

(33) Mahmood, J.; Kim, D.; Jeon, I.-Y.; Lah, M. S.; Baek, J.-B. Scalable Synthesis of Pure and Stable Hexaaminobenzene Trihydrochloride. *Synlett* **2013**, *24*, 246–248.